Supplementary Information

Electrodeposition of oxyanion films as universal chloride ions-repelling layers for efficient and stable seawater oxidation at ampere-level current density

Meng Zhang[a], Yuzhuo Sun[a], Chenchen Meng[a], Qijun Xu[a], Yang Zhang[a], Xiaohong Li[a], Louzhen Fan[a], Tengfei Li*[b], Yunchao Li*[a]

a. Key laboratory of Theoretical and Computational Photochemistry, Ministry of Education
College of Chemistry, Beijing Normal University, Beijing 100875 (P. R. China)
b. School of Chemistry and Environment, Manchester Metropolitan University, Manchester, M1 5GD, United Kingdom.
E-mail: liyc@bnu.edu.cn or t.li@mmu.ac.uk

Table of contents

electrodes. (e) The Cdl of NiCo-LDH, NiCo-LDH@Sulfate, NiCo-LDH@Phosphate and NiCo-LDH@Carbonate.

Fig. S15. TOF of NiCo-LDH@Sulfate, NiCo-LDH@Phosphate, NiCo-LDH@Carbonate and NiCo-LDH.

Fig. S16. (a-d) ClOR-LSV curves of NiCo-LDH electrodes modified with different oxyanions obtained through three repeated CLOR tests.

Fig. S17. Multistep chronoamperometry tests (MCT): (a-d) Current-time (I-t) curves for NiCo-LDH@Sulfate and other control electrodes recorded at different applied potentials in 3 M NaCl (from 1.324 V vs. RHE to 1.824 V vs. RHE).

Fig. S18. Steady-state Tafel studies for different catalysts in 3 M NaCl according to the multistep chronoamperometry tests displayed in Fig. S16.

Fig. S19. FE_{O2} for NiCo-LDH@Sulfate and other control electrodes measured at a fixed current density of 600 mA cm^{-2} in 1 M KOH + seawater.

Fig. S20. LSV curves of NiCo-LDH@Sulfate before and after 10000 CV cycles.

Fig. S21. Characterization of NiCo-LDH@Sulfate before and after 10000 CV cycles: XRD pattern (a), SEM images (b-c), Raman spectra (d).

Fig. S22. The XPS spectra of NiCo-LDH@Sulfate before and after stability testing: Ni 2p (a), Co 2p (b), O 1s (c) and S 2p (d).

Fig. S23. (a) HAADF image of NiCo-LDH@Sulfate after OER testing. (b-f) EDX-mapping images of NiCo-LDH@Sulfate after stability testing.

Fig. S24. (a-c) In-situ Raman spectra for NiCo-LDH@Sulfate (a), NiCo-LDH@Phosphate (b) and NiCo-LDH@Carbonate (c) in 1 M KOH + seawater.

Fig. S25. (a-d) Atomic models for NiCo-LDH (a), NiCo-LDH@Sulfate (b), NiCo-LDH@Phosphate (c) and NiCo-LDH@Carbonate (d).

Fig. S26. The adsorption model of NiCo-LDH depicting the binding of intermediates at each step.

Fig. S27. The adsorption model of NiCo-LDH@Sulfate depicting the binding of intermediates at each step.

Fig. S28. LSV curves of NiCo-LDH@Sulfate and NiCo-LDH in 1 M KOH electrolyte.

Fig. S29. (a-b) Atomic models for NiCoOOH (a) and NiCoOOH@Sulfate (b).

Fig. S30. (a) Gibbs free energy diagrams for NiCoOOH and NiCoOOH@Sulfate in OER and ClOR.

Fig. S31. (a-b) In-situ infrared spectra for NiCo-LDH (a) and NiCo-LDH@Sulfate (b) in 1 M KOH + seawater, highlighting the absorption band of *OH.

Fig. S32. (a-b) In-situ infrared spectra of NiCo-LDH (a) and NiCo-LDH@sulfate (b) at 0.8 V (vs. RHE) with highlighting the absorption band of *OH.

References

Experimental Procedures

Materials

Cobaltous (II) nitrate hexahydrate ($Co(NO_3)_2 \cdot 6H_2O$, 99%), nickel (II) nitrate hexahydrate ($Ni(NO_3)_2 \cdot 6H_2O$, 99%), iron (III) nitrate nine hydrate ($Fe(NO_3)_3 \cdot 9H_2O$, 99%), hexadecyltrimethylammonium bromide ($C_{19}H_{42}BrN$, 99%), urea ($CO(NH_2)_2$, 99%), ammonium fluoride (NH_4F, 98%), sodium sulfate (Na_2SO_4, 99%), sodium dihydrogen phosphate (NaH_2PO_4, 99%) and sodium bicarbonate ($NaHCO_3$, 99%) were purchased from Sinopharm Group Chemical Co., Ltd. Methanol (CH_3OH, 99.5%) and acetone (CH_3COCH_3, 99.5%) were purchased from Macklin reagent Co., Ltd. Hydrochloric acid (HCl, 38%), sodium hydroxide (KOH, 85%) were purchased from the Shanghai Chemical Plant. Nickel foam (NF) was obtained from CeTech Taiwan. Natural seawater come from the Yellow Sea, China. All chemicals were used without further purification or treatment.

Material Characterizations

Scanning electron microscopy (SEM) images were acquired using a Hitachi SU-8000 field-emission scanning electron microscope equipped with an energy-dispersive X-ray (EDX) spectroscopy detector (Oxford), operating at an acceleration voltage of 5 and 20 kV, respectively. Scanning transmission electron microscopy (STEM) and transmission electron microscopy (TEM) imaging were carried out with an FEI-F20 field-emission transmission electron microscope (FE-TEM). The specimens for TEM observations were scratched from the NF supports and sonicated before dropping them onto 200 mesh carbon-coated copper grids. To analyze the surface composition and elemental oxidation states of samples, X-ray photoelectron spectroscopy (XPS) measurements were carried out using a PHI5000 VersaProbe (ULVAC-PHI) spectrometer with a hemispherical energy analyzer, employing a monochromatized microfocused Al-Kα (hv = 1486.58 eV) X-ray source. The binding energies (BEs) of the core levels were calibrated by setting the adventitious C 1s peak at 284.8 eV. The X-ray diffraction (XRD) patterns were recorded using a Rigaku SmartLab diffractometer with a Cu Kα X-ray source (λ = 1.5406 Å, generated at 40 kV and 100 mA) at a scanning rate of 0.06° s^{-1}, and scanned in the Bragg–Brentano mode from 2θ of 10° to 80° in 0.02° increments. The NF sheets coated with an active material were directly used as the specimens for XRD characterization after cleaning treatment. The chemical compositions of the catalysts were determined by EDX quantitative analysis measurements after dissolving them in aqua regia. In situ Raman spectra were collected by using a Jobin-Yvon LabRAM HR800 Raman spectrometer (excitation wavelength: 532 nm). And In situ FTIR measurements were conducted using a TENSOR II FTIR spectrophotometer equipped with a silicon crystal attenuated total reflectance (ATR) accessory. CHI 760e electrochemical workstation was used for all electrochemical testings, the modified NF electrodes were employed as the working electrodes, with

Hg/HgO and a carbon rod serving as the reference and counter electrode, respectively. In situ Raman and FTIR spectra were acquired under different applied potentials. For TOF-SIMS measurements, all control electrodes were electrochemically activated in alkaline seawater before testing. Additionally, negative TOF-SIMS counts were collected from m/z = 96/95/60 (SO_4^{2-}, PO_4^{3-}, and CO_3^{2-}) after Ar plasma milling for 5 to 15 minutes to clean the surface of adsorbed electrolytes, and average TOF-SIMS anion counts within the test area were collected (Scale bars: 100 μm).

Electrochemical Measurements

All electrochemical measurements were carried out on a CHI 760e electrochemical workstation. The working electrodes were 0.5×1 cm^2 oxyanion-modified NF electrodes, the counter electrode was carbon rod, the reference electrode was Hg/HgO electrode in seawater containing 1 M KOH (pH = 14). The experiments were carried out in two-electrode or three-electrode system. Liner sweep voltammetry (LSV) polarization curves were tested in the voltage range of 0 V to 1 V (vs. RHE) in seawater containing 1 M KOH. The potential of the reversible hydrogen electrode (RHE) can be calculated using the following formula:

$E_{RHE} = E_{Hg/HgO} + 0.059*pH+0.098$

Where E_{RHE} is the potential relative to the reversible hydrogen electrode, 0.059 is a constant representing the change in potential per pH unit at 25°C (298 K), with units in V/pH, and the pH of alkaline seawater is 14.

Faradaic efficiency calculation (FE%): FE% was calculated using the following equation:

$FE\% = V_g(experimental)/V_g(theoretical)$

where V_g(experimental) represents the volume of gas actually produced, and V_g(theoretical) is the theoretical gas volume calculated based on Faraday's law. Specifically, V_g(theoretical) = Q/zF, where Q is the total charge passed through the electrodes, z means z mole electrons per mole O_2 (z = 4), and F is Faraday's constant (96500 C mol^{-1}).

Turnover frequency (TOF) calculation: TOF value for each catalyst was calculated based on the following equation:

TOF = # total oxygen turnover per cm^2 geometric area / # active sites per cm^2 geometric area

Specifically, the number of total oxygen turnover per cm^2 is obtained using the following formula:

O_2 = (j mA/cm^2) (1 C s^{-1}/1000 mA) (1 mol O_2/4 mol e^-) (6.02 * 10^{23} molecules O_2/1 mol O_2) = 1.56 * 10^{15} O_2 S^{-1}/cm^2 per mA/cm^2

Considering that surface Ni sites are generally recognized as the primary active sites in most NiFe- and NiCo-based compounds for the OER, we referenced previous studies and assumed that the total number of surface Ni sites corresponds to the number of active sites.[1] Molar mass of Ni: 58.69 g mol^{-1};

Density of Ni: 8.90 g cm^{-3}; Molar volume of Ni: 6.60 cm^3 mol^{-1}. The average number of surface atoms per square centimeter:

surface sites = (6.02 * 10^{23} atoms/1 mol * 1mol/6.60 cm^3)$^{2/3}$ = 2.03 * 10^{15} atoms/cm^2

Then, the current density from the LSV polarization curves can be converted into TOF values according to the following equation:

TOF = (1.56 * 10^{15} O_2 S^{-1}/cm^2 per mA/cm^2) * |j|/(# surface sites) * A_{ECSA}

The amperometric current density-time (i-t) curve was also measured in seawater containing 1 M KOH. The polarization curves of 10000 CV cycles for OER were carried out in seawater containing 1 M KOH. The voltage range was 1 V to 2 V (vs. RHE). Carbon rods were used as the counter electrodes in the CV cycling tests. Electrochemical impedance spectra (EIS) were measured at the potential of 1.123 V (vs. RHE) in the frequency range from 10 kHz to 0.04 Hz. The electrochemical surface areas (ECSAs) were obtained by the double-layer capacitance (C_{dl}), which was measured in non-Faraday region by cyclic voltammetry (CV). This non-Faraday region is usually located around the open circuit potential, where all measured currents are attributed to double-layer charging.[2] The CV data collected here were scanned from 0.724 to 0.824 V (vs. RHE) at various scan rates ranging from 20 to 100 mV s^{-1}. To analyze the electrolysis products, an H-shaped cell with a volume of 40 mL was utilized, incorporating with anion exchange membranes (obtained from Versogen, United States). After electrolysis, the electrolytes were analyzed for hypochlorous acid formation using iodometric titration. Specifically, aliquots of the electrolytes were extracted after 1 hour of chronoamperometric testing, freshly prepared 0.5 M potassium iodide (KI) and starch were added to the solution, leading to the formation of a dark red complex, indicative of the presence of hypochlorous acid. This solution was then titrated with 0.01 M sodium thiosulfate ($Na_2S_2O_3$) until it became colorless, enabling the calculation of hypochlorous acid concentration in the solution. Notably, TOF-SIMS measurements were also utilized for accurate quantification of the ClO^- on the surfaces of the electrodes after electrochemical activation in alkaline seawater.

Computational Details

For the material models simulated in this study, periodic boundary conditions were applied in the x, y, and z dimensions. The OPLS force field, which is suitable for electrolyte solution, was used to optimize sample structures for preliminary structural optimization. Atomic charges of ions were multiplied by scale factor 0.73 to correct the polarization effects of anion and cation. First, the conjugate gradient algorithm and energy minimization were performed to obtain a stable structure before using dynamic simulations. Each sample was then equilibrated under the NPT ensemble at a constant temperature of

400 K to achieve an equilibrium state with zero pressure for 5 ns. Subsequently, the system temperature was reduced from 400 K to 298 K for annealing 5 ns under the NPT ensemble (under 1 atmosphere pressure). The Andersen feedback thermostat and Berendsen barostat algorithm were applied in the system with temperature and pressure conversion. Next, MD simulations were further carried out for 10 ns with a time step of 1 fs per integration step under the ensemble conditions of NVT (298 K). System energy can be obtained through structural optimization using the energy minimization.

We employed the Vienna Ab Initio Package (VASP)[3-4] to perform all the density functional theory (DFT) calculations within the generalized gradient approximation (GGA) using the PBE[5] formulation. We chose the projected augmented wave (PAW) potentials[6-7] to describe the ionic cores and take valence electrons into account using a plane wave basis set with a kinetic energy cutoff of 450 eV. Partial occupancies of the Kohn-Sham orbitals were allowed using the Gaussian smearing method and a width of 0.05 eV. The electronic energy was considered self-consistent when the energy change was smaller than 10-6 eV. A geometry optimization was considered convergent when the force change was smaller than 0.03 eV/Å. Grimme's DFT-D3 methodology[8] was used to describe the dispersion interactions. The vacuum spacing perpendicular to the plane of the structure is 15 Å. The Brillouin zone integral used the surfaces structures of 2×2×1 monkhorst pack K point sampling. The free energy was calculated as follows:

$$G = E + ZPE - TS$$

where G, E, ZPE and TS are the free energy, total energy from DFT calculations, zero-point energy and entropic contributions, respectively.

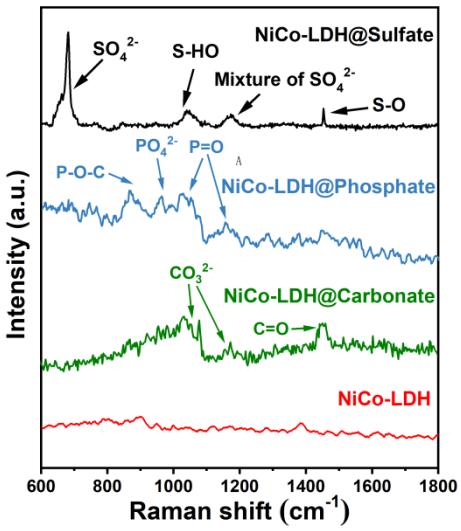

Fig. S1. Raman spectra of NiCo-LDH, NiCo-LDH@Sulfate, NiCo-LDH@Phosphate and NiCo-LDH@Carbonate.

We characterized catalysts NiCo-LDH@Sulfate, NiCo-LDH@Phosphate and NiCo-LDH@Carbonate using Raman spectroscopy. Vibration peaks of SO_4^{2-}, PO_4^{3-}, and CO_3^{2-} were observed at 685.36, 958.96 and 1027.63 cm^{-1}, respectively, confirming the presence of corresponding oxyanion films on the surfaces of the three catalysts mentioned above.[9-10] This also indicates that we have successfully deposited the oxyanion films on the surface of NiCo-LHD.

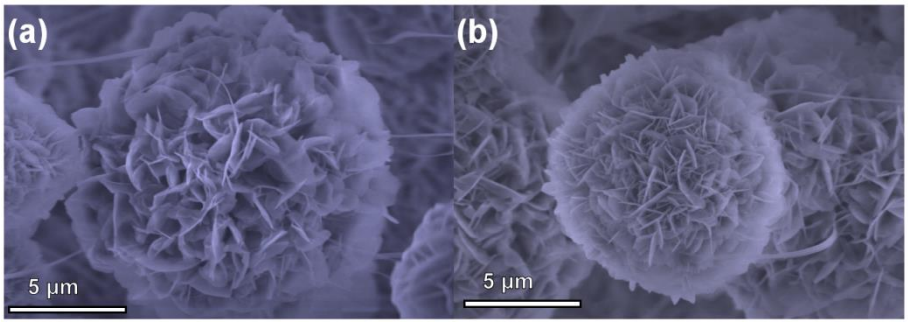

Fig. S2. SEM images of (a) NiCo-LDH@Phosphate and (b) NiCo-LDH@Carbonate.

We observed through SEM that the surface morphology of NiCo-LDH remained almost unchanged after surface modification with phosphate and carbonate. This indicates that our electrodeposition surface modification strategy has milder reaction conditions compared to other strategies (solvothermal method, chemical vapor deposition method, etc.), which can effectively avoid metal aggregation and surface morphology collapse caused by high temperature, and help to maintain the activity of the catalyst.[11-12]

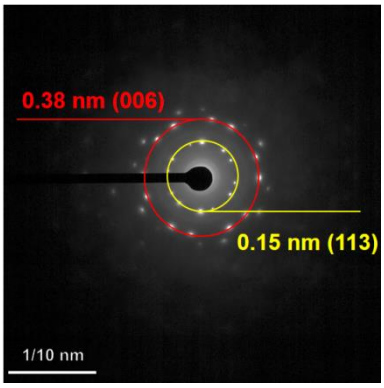

Fig. S3. SAED pattern of NiCo-LDH@Sulfate.

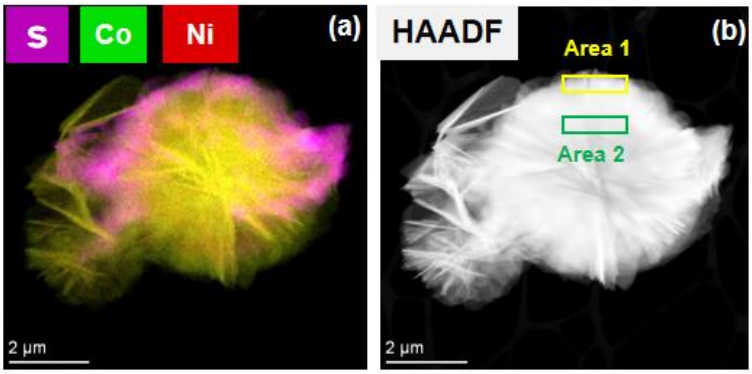

Fig. S4. (a) Total EDX-mapping of NiCo-LDH@Sulfate. (b) HAADF image of NiCo-LDH@Sulfate (Refer to Table S1 for Region 1 and Region 2 analysis).

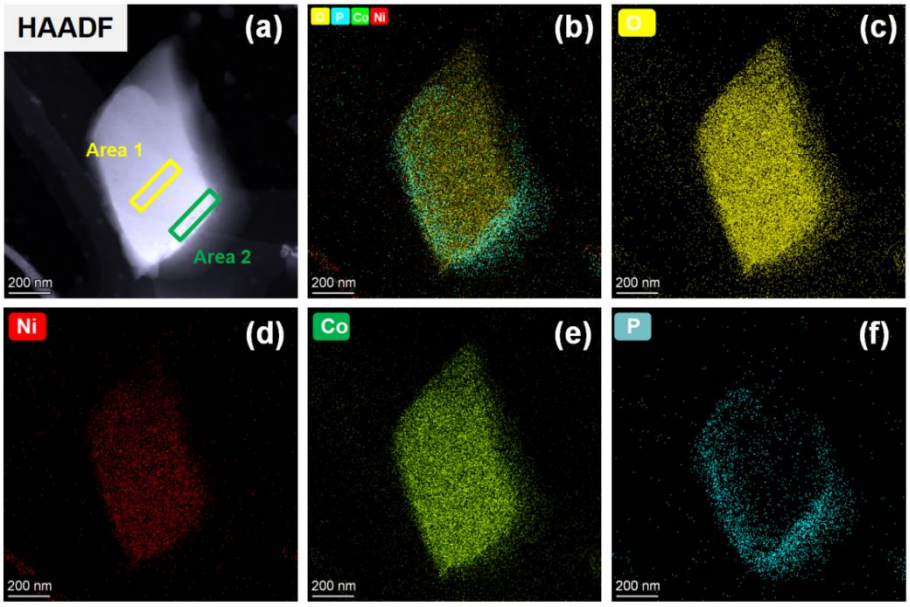

Fig. S5. (a) HAADF image of NiCo-LDH@Phosphate. (b) Total EDX-mapping of NiCo-LDH@Phosphate. (c-f) EDX-mapping of O elemental (c), Ni elemental (d), Co elemental (e) and P elemental(f).

The energy dispersive X-ray (EDX) mapping image shows the uniform distribution of Ni, Co, and O elements in NiCo-LDH@Phosphate, while P element is mainly distributed outside the sheet-like structure. In addition, we also analyzed the element content of the inner and outer structures of the core-shell structure (Table S2), confirming that NiCo-LDH@Phosphate was successfully synthesized.

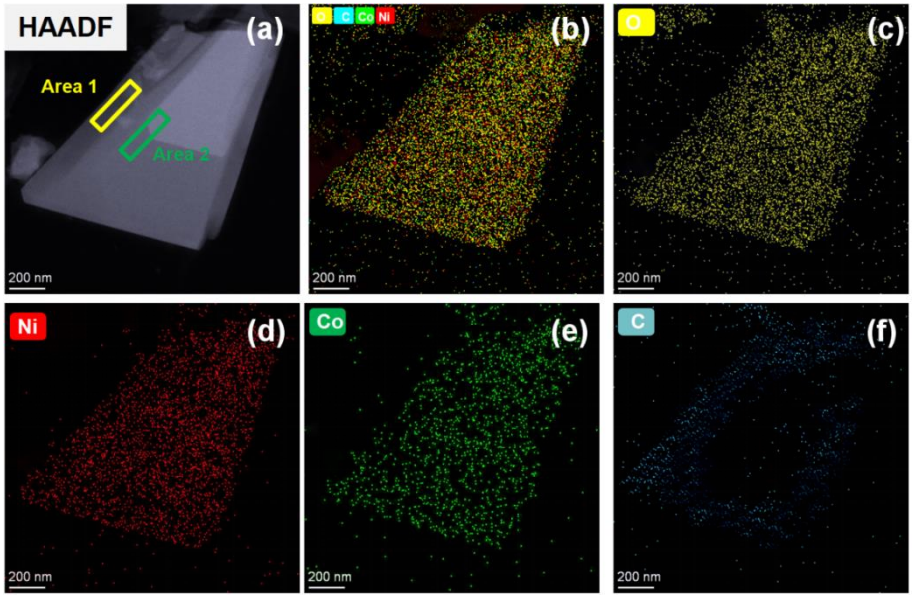

Fig. S6. (a) HAADF image of NiCo-LDH@Carbonate. (b) Total EDX-mapping of NiCo-LDH@Carbonate. (c-f) EDX-mapping of O elemental (c), Ni elemental (d), Co elemental (e) and C elemental (f).

EDX-mapping images reveal a uniform distribution of Ni, Co, and O elements in NiCo-LDH@Carbonate, while the C element is primarily distributed on the exterior of the sheet-like structure. Additionally, we analyzed the elemental content of the inner and outer regions of the core-shell structure, as shown in Table S3. These results confirm the successful synthesis of NiCo-LDH@Carbonate.

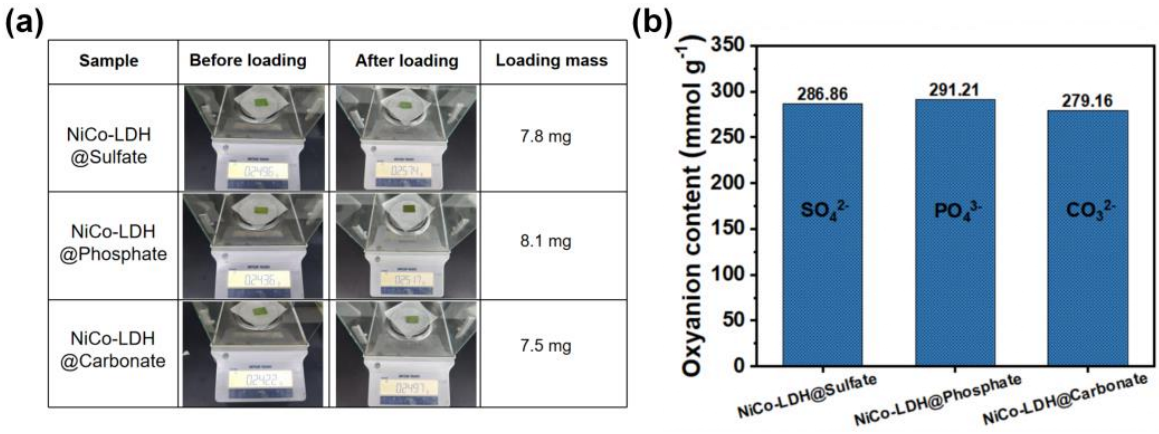

Fig. S7. (a) Comparison of oxyanion loading between NiCo-LDH@Sulfate, NiCo-LDH@Phosphate and NiCo-LDH@Carbonate. (b) oxyanion contents on the surfaces of NiCo-LDH@Sulfate, NiCo-LDH@Phosphate, and NiCo-LDH@Carbonate determined by Ion chromatography analysis.

We measured the mass differences of the electrodes before and after electrodeposition of various oxyanion films, and the results indicate that the loading differences between the electrodes are minimal (less than 0.006 g). Furthermore, the oxyanion contents of NiCo-LDH@Sulfate, NiCo-LDH@Phosphate, and NiCo-LDH@Carbonate were evaluated by ion chromatography analysis. The sulfate content in NiCo-LDH@Sulfate is 286.86 mmol g^{-1}, the phosphate content in NiCo-LDH@Phosphate is 291.21 mmol g^{-1}, and the carbonate content of NiCo-LDH@Carbonate is 279.16

mmol g^{-1}. Evidently, the differences in the oxyanion contents in the three types of electrodes are quite small.

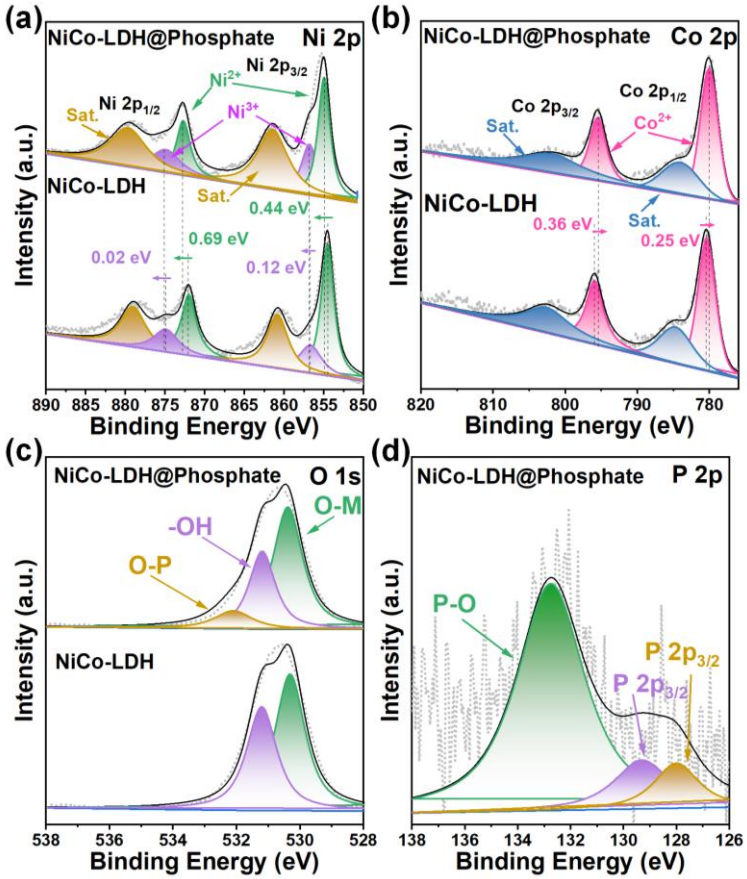

Fig. S8. High-resolution XPS spectra of NiCo-LDH@Phosphate and NiCo-LDH: Ni 2p (a), Co 2p (b), O 1s (c) and P 2p (d), respectively.

In the high-resolution XPS spectrum of Ni 2p (**Fig.** S8a), after surface modification with phosphate film, both the peak of Ni^{2+} (Ni $2p_{3/2}$ at 854.80 eV, Ni $2p_{1/2}$ at 872.65 eV) and Ni^{3+} (Ni $2p_{3/2}$ at 856.73 eV, Ni $2p_{1/2}$ at 874.84 eV) in Ni 2p shift to higher binding energies. In contrast, **Fig.** S8b shows that in the Co 2p spectrum, the peak of Co^{2+} (Co $2p_{3/2}$ at 780.12 eV and Co $2p_{1/2}$ at 795.56 eV) shift to lower binding energies. Additionally, the O 1s spectrum displays a new O-P feature peak (532.15 eV) after phosphate film modification, (**Fig.** S8c) while the P 2p spectrum is dominated by P-O feature peak (132.72 eV). We also observed characteristic peaks for P $2p_{1/2}$ (129.32 eV) and P $2p_{3/2}$ (127.97 eV), which result from the bonding between P and the NiCo-LDH surface metals. (**Fig.** S8d) This result is similar to the XPS spectrum of NiCo-LDH@Sulfate, which can be attributed to the regulation of the catalyst's electronic structure by phosphate film modification, enhancing electron transfer from Ni to Co.

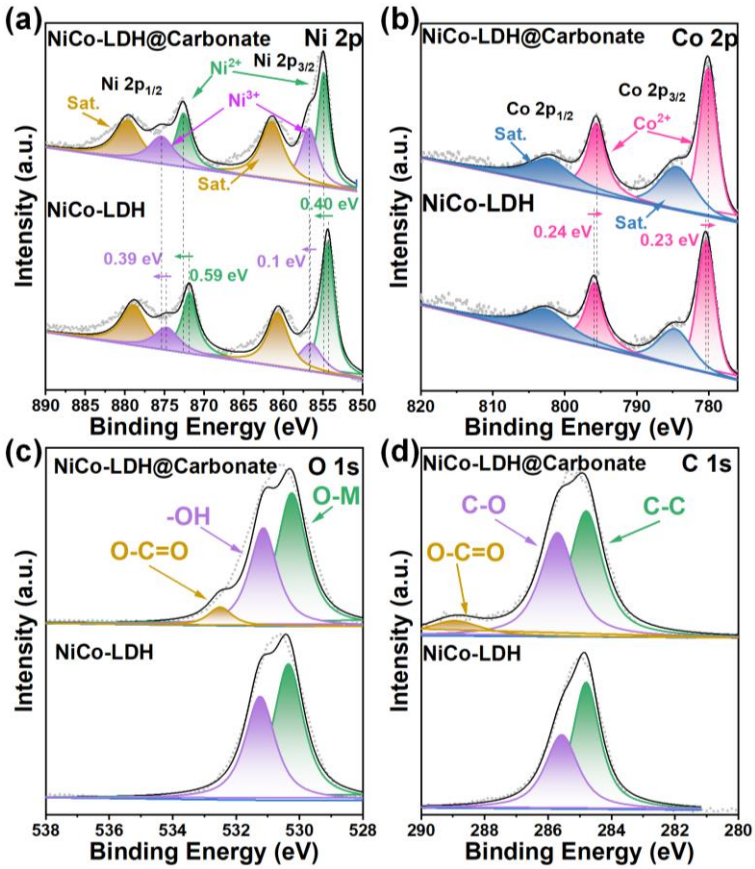

Fig. S9. High-resolution XPS spectra of NiCo-LDH@Carbonate and NiCo-LDH: Ni 2p (a), Co 2p (b), O 1s (c) and C 1s (d), respectively.

In the high-resolution XPS spectrum of Ni 2p (**Fig.** S9a), after surface modification with carbonate film, both the peak of Ni^{2+} (Ni $2p_{3/2}$ at 854.76 eV, Ni $2p_{1/2}$ at 872.55 eV) and Ni^{3+} (Ni $2p_{3/2}$ at 856.71 eV, Ni $2p_{1/2}$ at 875.21 eV) in Ni 2p shift to higher binding energies. In contrast, **Fig.** S9b shows that in the Co 2p spectrum, the peak of Co^{2+} (Co $2p_{3/2}$ at 780.14 eV and Co $2p_{1/2}$ at 795.68 eV) shift to lower binding energies. Additionally, after carbonate film modification, the O 1s spectrum displays a new O-C=O feature peak at 532.51 eV (**Fig.** S9c), and the C 1s spectrum also shows an O-C=O feature peak at 288.98 eV (**Fig.** S9d). This result is similar to the XPS spectrum of NiCo-LDH@Sulfate and can be attributed to the regulation of the catalyst's electronic structure by carbonate film modification, enhancing electron transfer from Ni to Co.

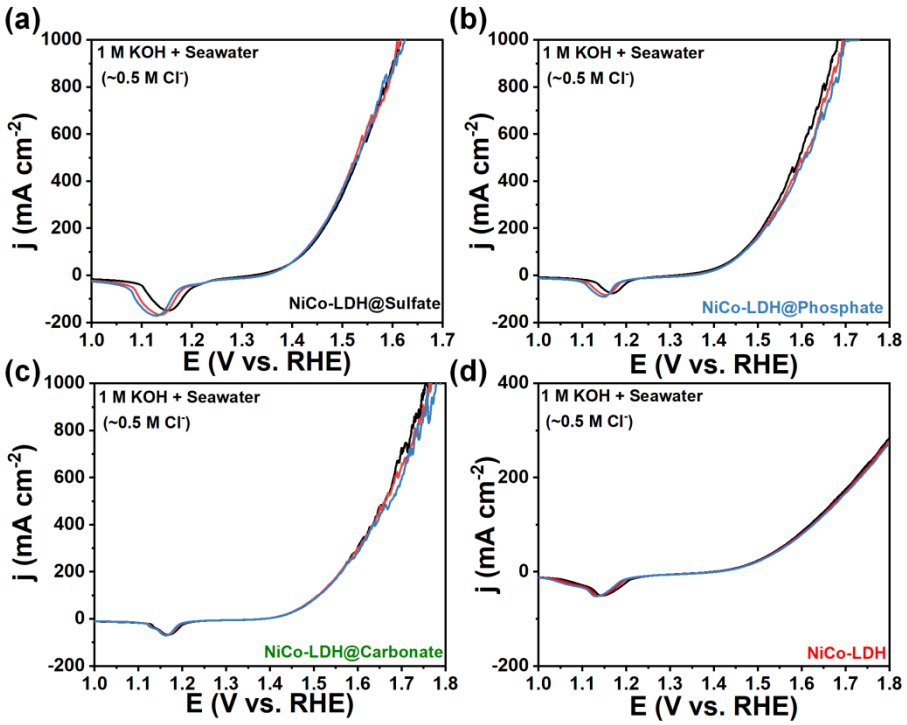

Fig. S10. (a-d) LSV curves of NiCo-LDH electrodes modified with different oxyanions obtained through three repeated OER tests.

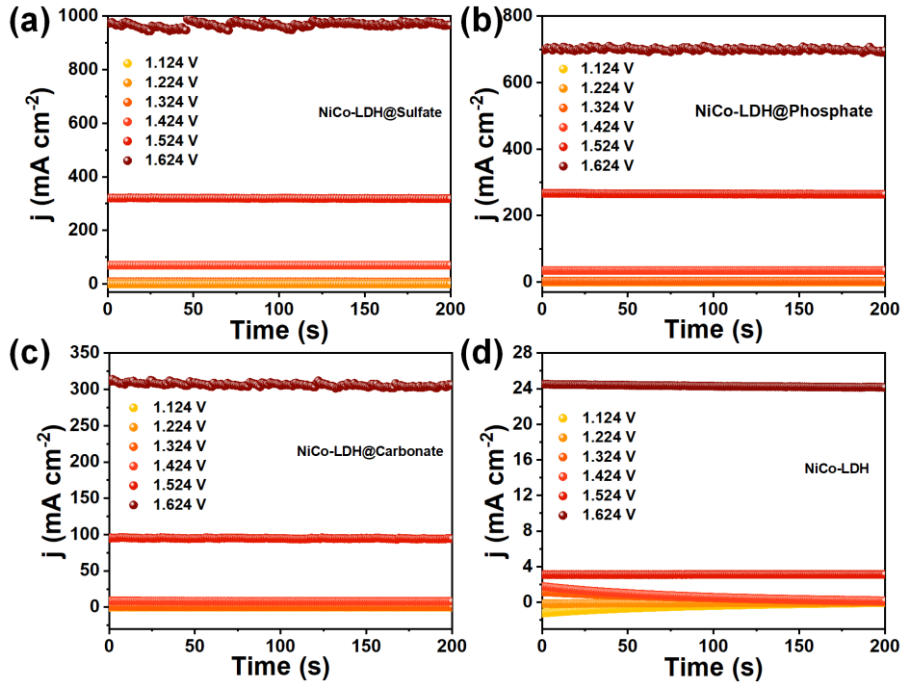

Fig. S11. Multistep chronoamperometry tests (MCT): (a-d) Current-time (I-t) curves for NiCo-LDH@Sulfate and other control electrodes recorded at different applied potentials in 1 M KOH + seawater (from 1.124 V vs. RHE to 1.624 V vs. RHE).

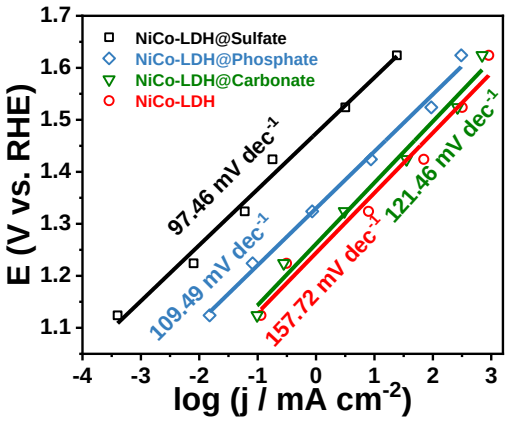

Fig. S12. Steady-state Tafel studies for different catalysts according to the multistep chronoamperometry tests displayed in Fig. S11.

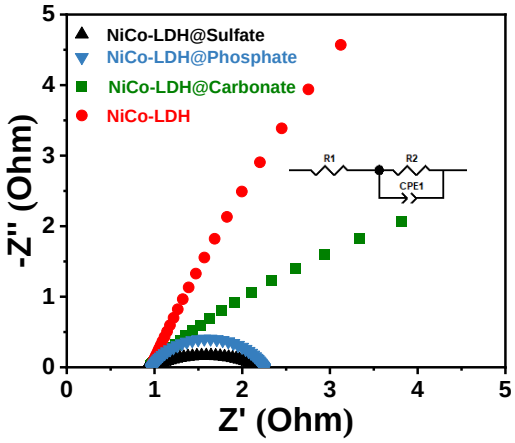

Fig. S13. (a) EIS spectra of NiCo-LDH, NiCo-LDH@Sulfate, NiCo-LDH@Phosphate and NiCo-LDH@Carbonate.

We conducted electrochemical impedance spectroscopy analysis on all electrodes (Fig. S13a), and the relevant Rct and Rs data are shown in Table S4, the NiCo-LDH@Sulfate has the lowest charge transfer resistance.

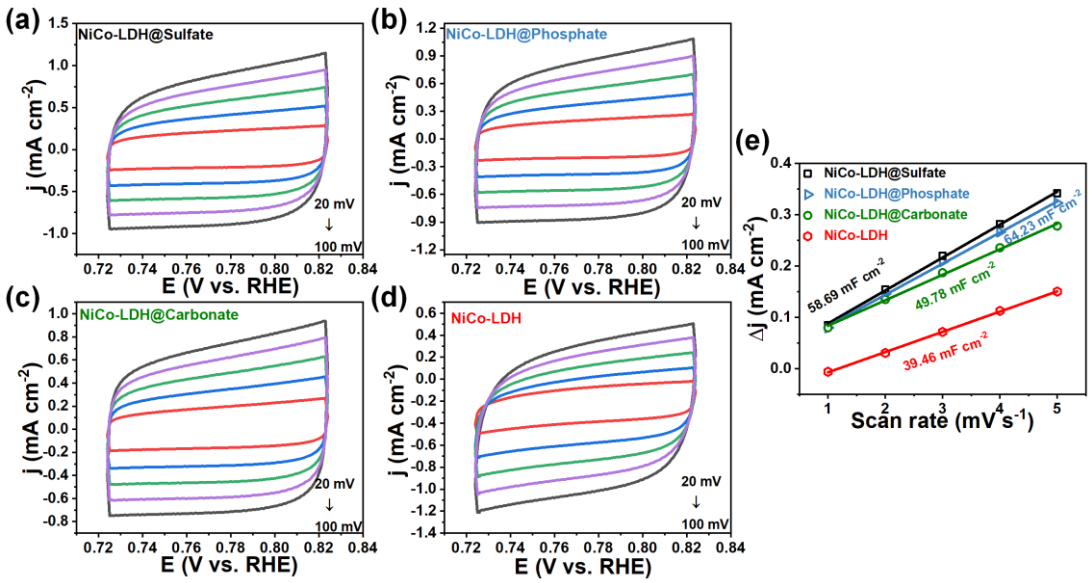

Fig. S14. (a-d) The CV curves under 20, 40, 60, 80 and 100 mV/s of NiCo-LDH, NiCo-LDH@Sulfate, NiCo-LDH@Phosphate NiCo-LDH@Carbonate to measure the electrochemical active surface areas for the electrodes. (e) The Cdl of NiCo-LDH, NiCo-LDH@Sulfate, NiCo-LDH@Phosphate and NiCo-LDH@Carbonate.

The electrochemical active surface areas (ECSA) of the catalysts were further evaluated using double-layer capacitance (C_{dl}) as an indicator. As shown in Fig. S14a-e, the Cdl value of NiCo-LDH@Sulfate is 58.69 mF cm^{-2}, superior than NiCo-LDH@Phosphate (64.23 mF cm^{-2}), NiCo-LDH@Carbonate (49.78 mF cm^{-2}) and NiCo-LDH (39.46 mF cm^{-2}).

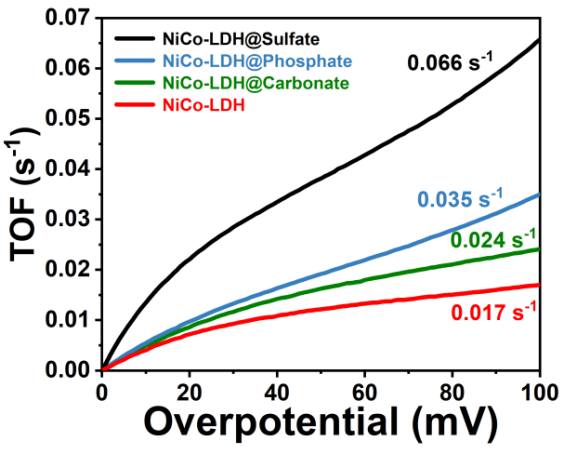

Fig. S15. TOF of NiCo-LDH@Sulfate, NiCo-LDH@Phosphate, NiCo-LDH@Carbonate and NiCo-LDH.

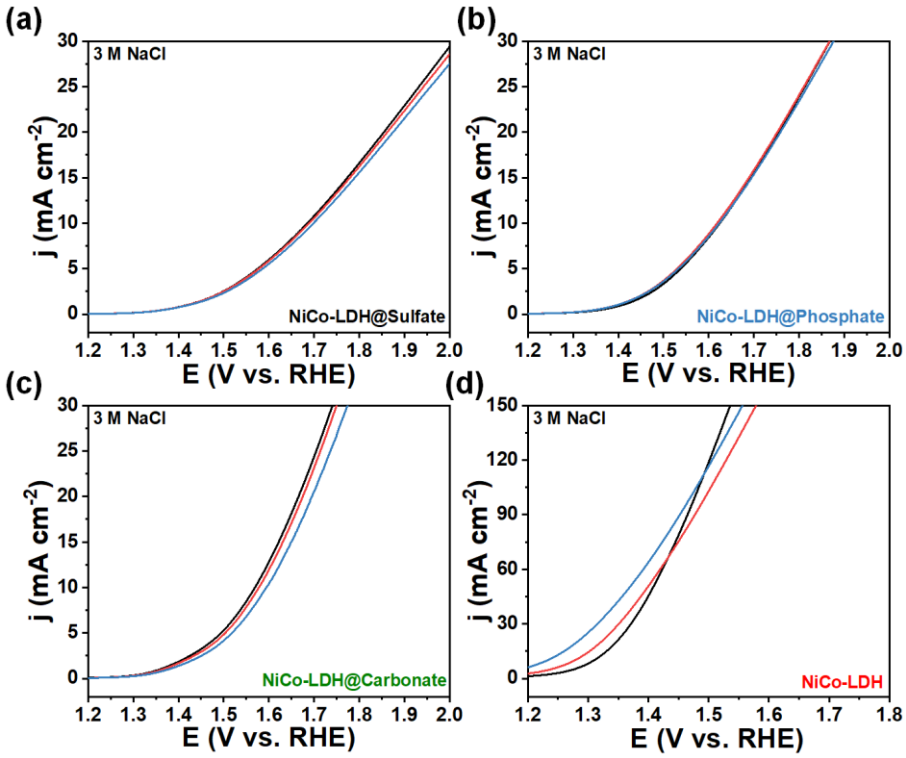

Fig. S16. (a-d) LSV curves of NiCo-LDH electrodes modified with different oxyanions obtained through three repeated CLOR tests.

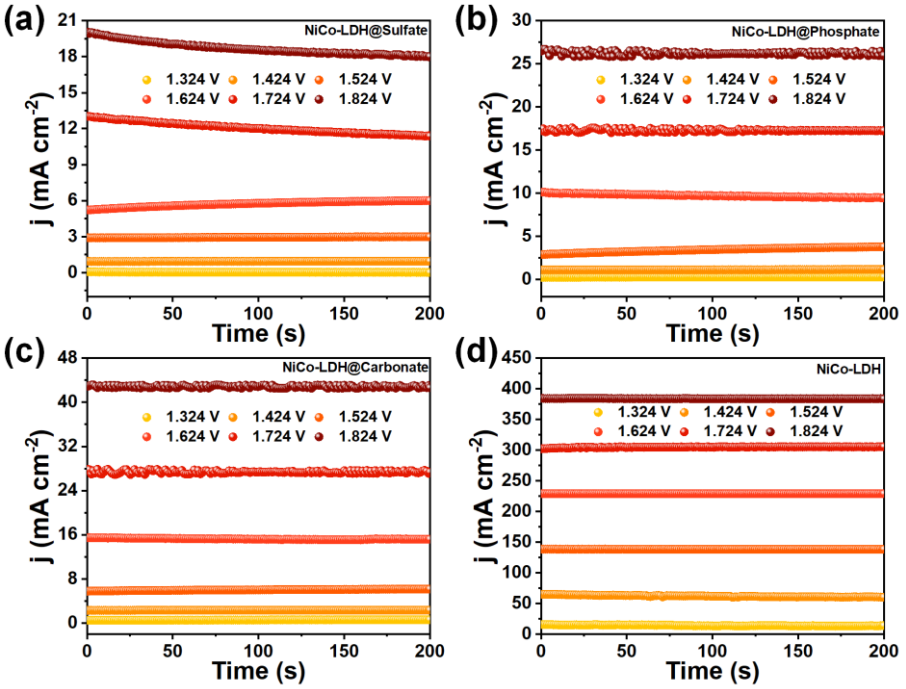

Fig. S17. Multistep chronoamperometry tests (MCT): (a-d) Current-time (I-t) curves for NiCo-LDH@Sulfate and other control electrodes recorded at different applied potentials in 3 M NaCl (from 1.324 V vs. RHE to 1.824 V vs. RHE).

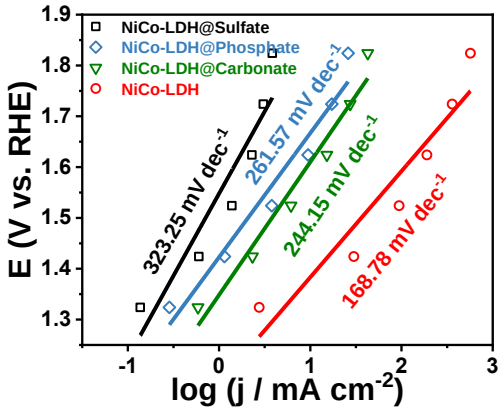

Fig. S18. Steady-state Tafel studies for different catalysts in 3 M NaCl according to the multistep chronoamperometry tests displayed in Fig. S17.

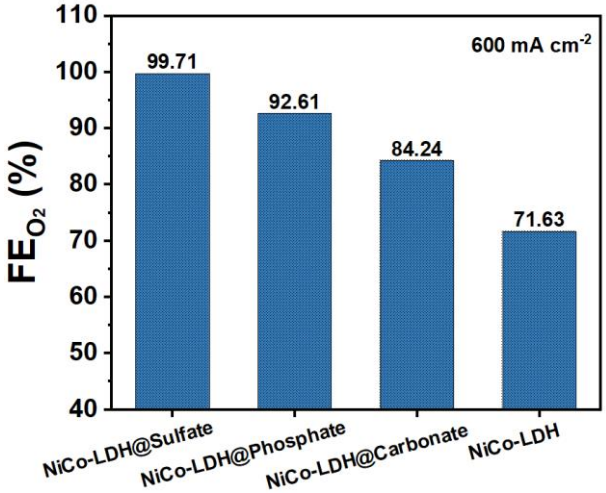

Fig. S19. FE_{O2} for NiCo-LDH@Sulfate and other control electrodes measured at a fixed current density of 600 mA cm^{-2} in 1 M KOH + seawater.

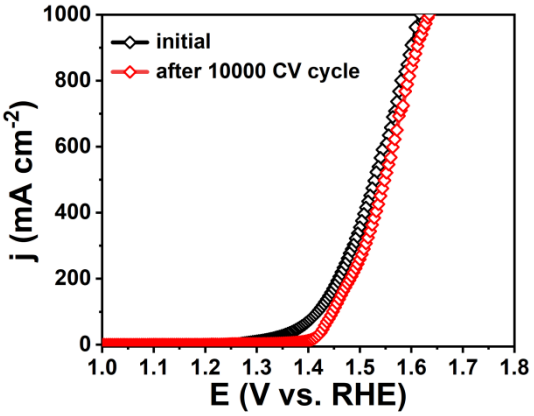

Fig. S20. LSV curves of NiCo-LDH@Sulfate before and after 10000 CV cycles.

After experiencing 10000 CV cycles, NiCo-LDH@Sulfate required 1.64 V to reach 1 A cm^{-2}, a mere 1.2% increase from its initial value of 1.62 V (before the test).

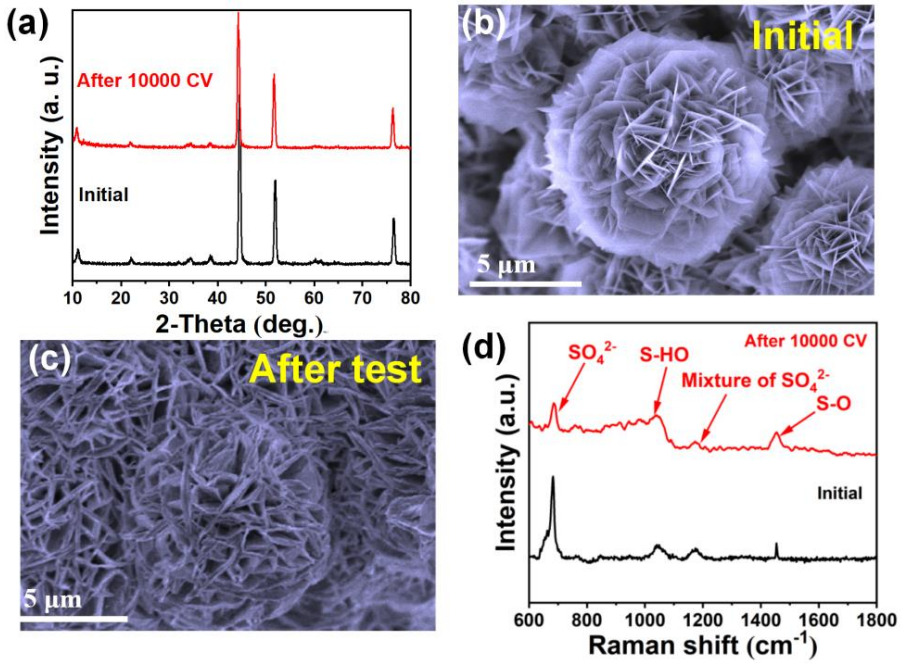

Fig. S21. Characterization of NiCo-LDH@Sulfate before and after 10000 CV cycles: XRD pattern (a), SEM images (b-c), Raman spectra (d).

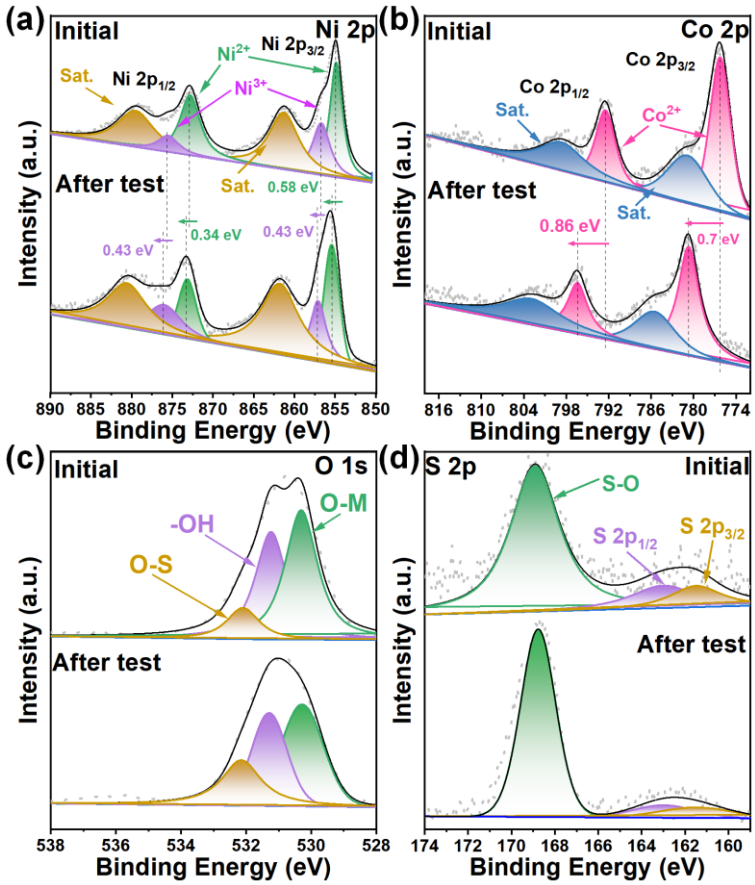

Fig. S22. The XPS spectra of NiCo-LDH@Sulfate before and after stability testing: Ni 2p (a), Co 2p (b), O 1s (c) and S 2p (d).

The high-resolution XPS spectrum of Ni 2p (Fig. S22a) reveals a positive shift of all characteristic peaks, accompanied by an enhancement in the relative intensity of Ni^{3+} peak. This observation indicates that a fraction of Ni^{2+} underwent oxidation to higher valence states during the stability testing process. A similar phenomenon is observed in the Co 2p spectrum (Fig. S22b), suggesting analogous oxidation behavior for cobalt ions. More importantly, quantitative analysis of the spectra (Table S7) disclosed that the contents of Ni, Co, and S elements exhibit only a minor decrease (< 11%) after the stability test, reconfirming the good compositional stability of NiCo-LDH@Sulfate.

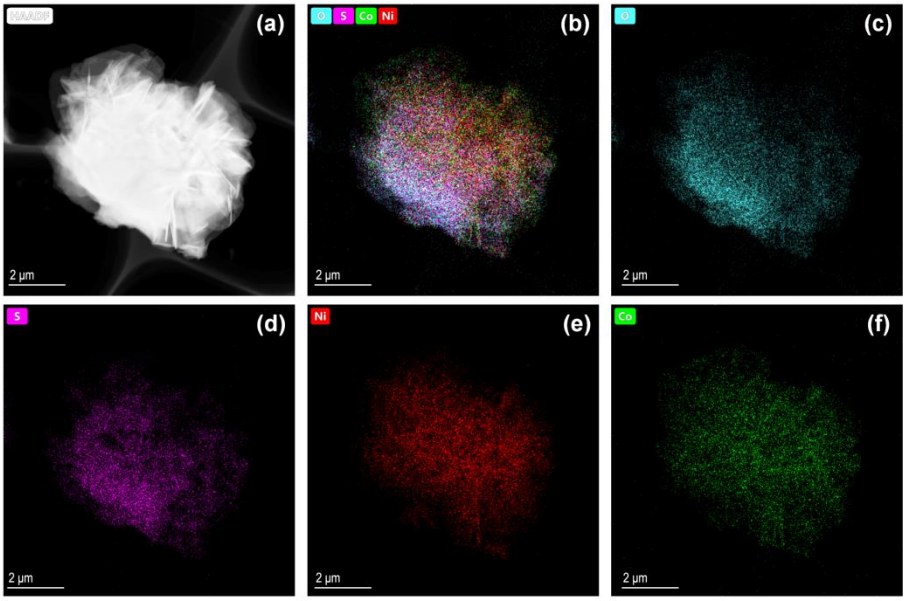

Fig. S23. (a) HAADF image of NiCo-LDH@Sulfate after OER testing. (b-f) EDX-mapping images of NiCo-LDH@Sulfate after stability testing.

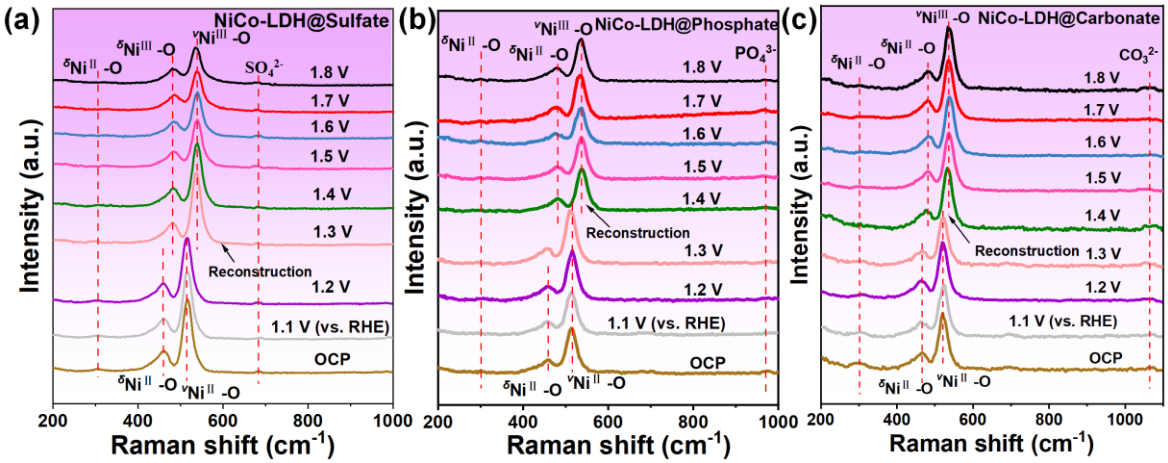

Fig. S24. (a-c) In-situ Raman spectra for NiCo-LDH@Sulfate (a), NiCo-LDH@Phosphate (b) and NiCo-LDH@Carbonate (c) in 1 M KOH + seawater.

In-situ Raman spectroscopy was used to monitor the structural evolution of NiCo-LDH@Phosphate and NiCo-LDH@Carbonate during seawater OER. As shown in Fig. S24b-c, characteristic peaks around 460 and 518 cm^{-1} can be attributed to the $^{\delta}Ni^{II}$-O and $^{\nu}Ni^{II}$-O vibration signals. As the reaction progresses, peaks corresponding to δNi^{III}-O (481.53 cm^{-1}) and $^{\nu}Ni^{III}$-O (541.82 cm^{-1}) appear at 1.4 V vs. RHE. In contrast, for NiCo-LDH@Sulfate (Fig. S24a), the in-situ reconstruction process is completed at a lower potential (1.3 V vs. RHE). The more facile formation of OER-active sites in NiCo-LDH@Sulfate likely contributes to its superior OER performance.

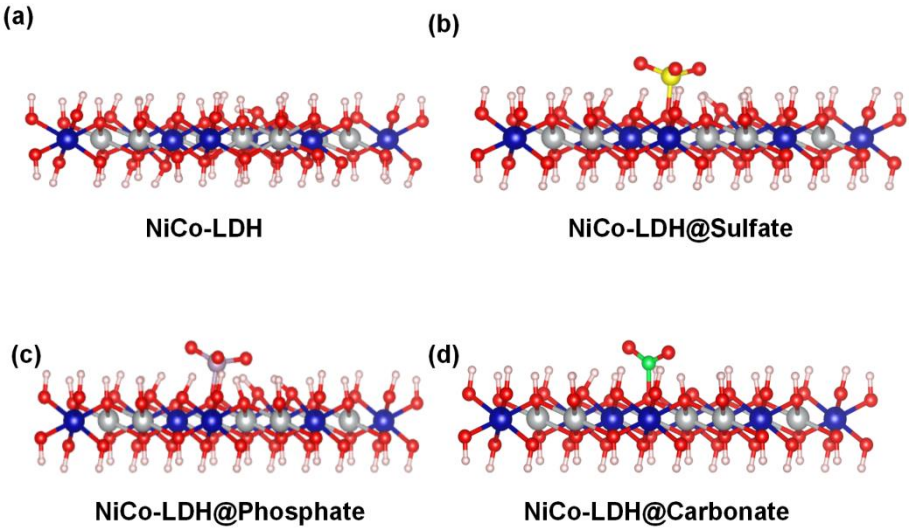

Fig. S25. (a-d) Atomic models for NiCo-LDH (a), NiCo-LDH@Sulfate (b), NiCo-LDH@Phosphate (c) and NiCo-LDH@Carbonate (d).

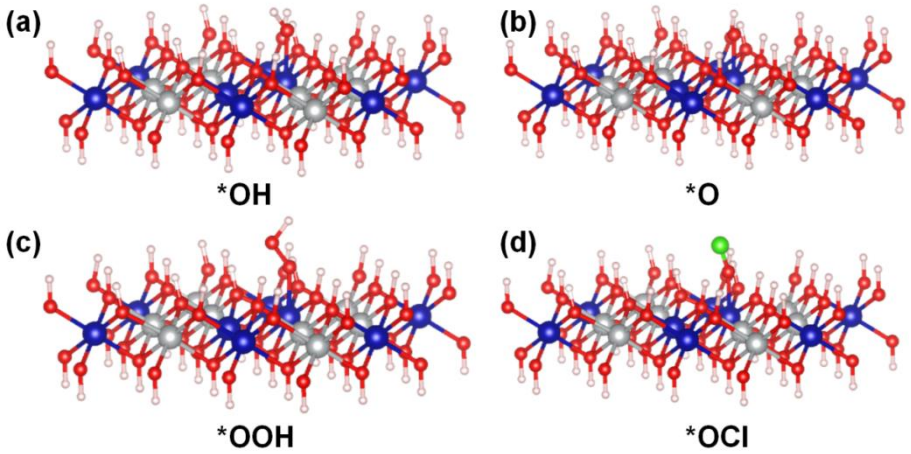

Fig. S26. The adsorption model of NiCo-LDH depicting the binding of intermediates at each step.

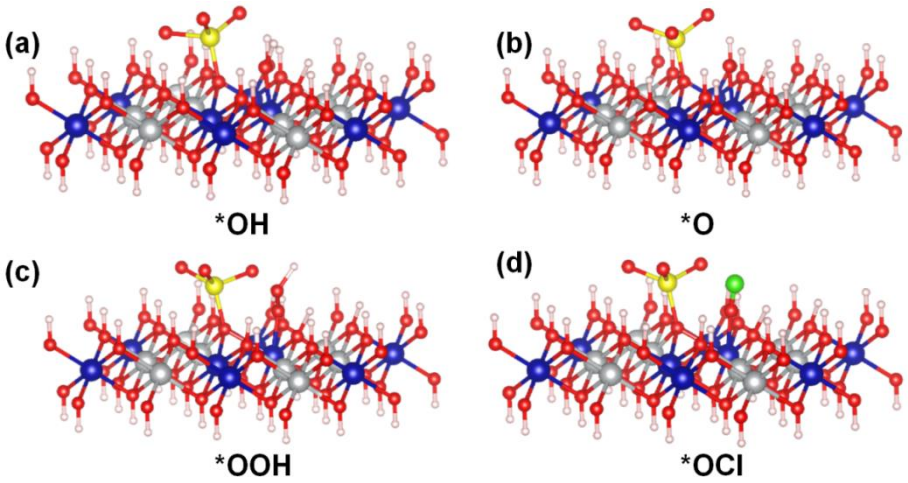

Fig. S27. The adsorption model of NiCo-LDH@Sulfate depicting the binding of intermediates at each step.

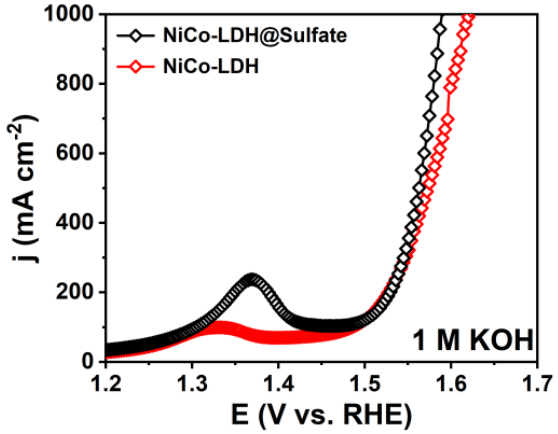

Fig. S28. LSV curves of NiCo-LDH@Sulfate and NiCo-LDH in 1 M KOH electrolyte.

Across the entire electrochemical window, NiCo-LDH@Sulfate exhibited outstanding OER activity in 1 M KOH, requiring only 360 mV to reach 1000 mA cm^{-2}, outperforming NiCo-LDH. The results indicate that NiCo-LDH@Sulfate can maintain higher OER activity than NiCo-LDH even without Cl^- interference.

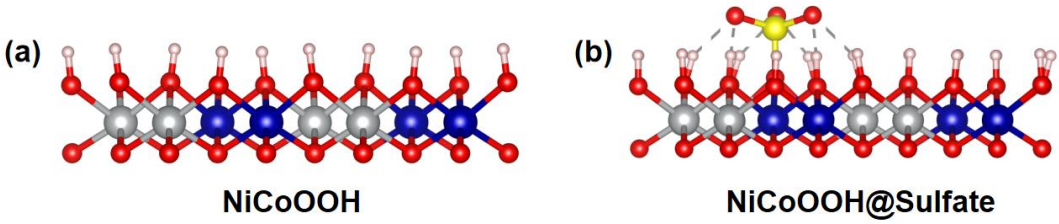

Fig. S29. (a-b) Atomic models for NiCoOOH (a) and NiCoOOH@Sulfate (b).

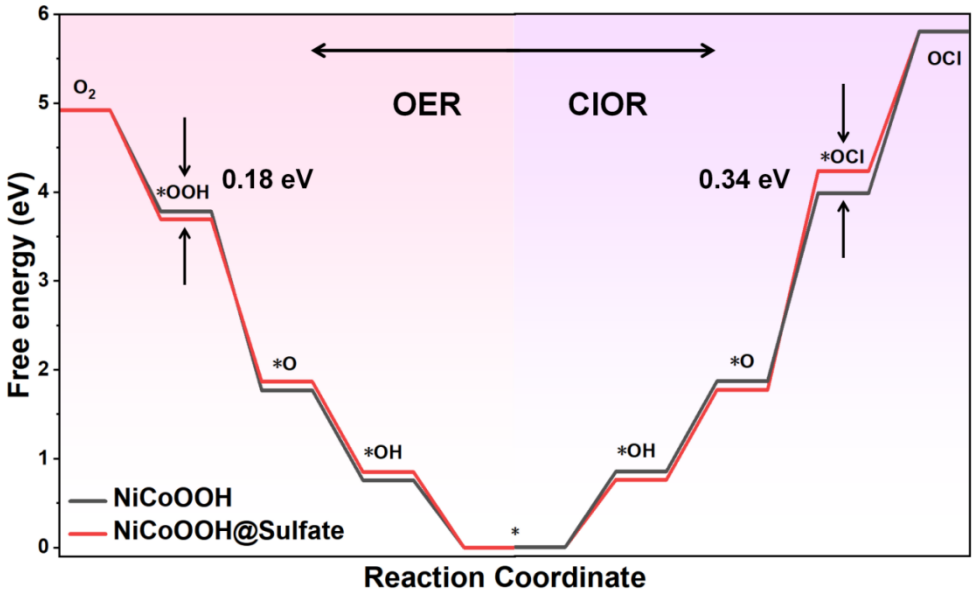

Fig. S30. (a) Gibbs free energy diagrams for NiCoOOH and NiCoOOH@Sulfate in OER and ClOR.

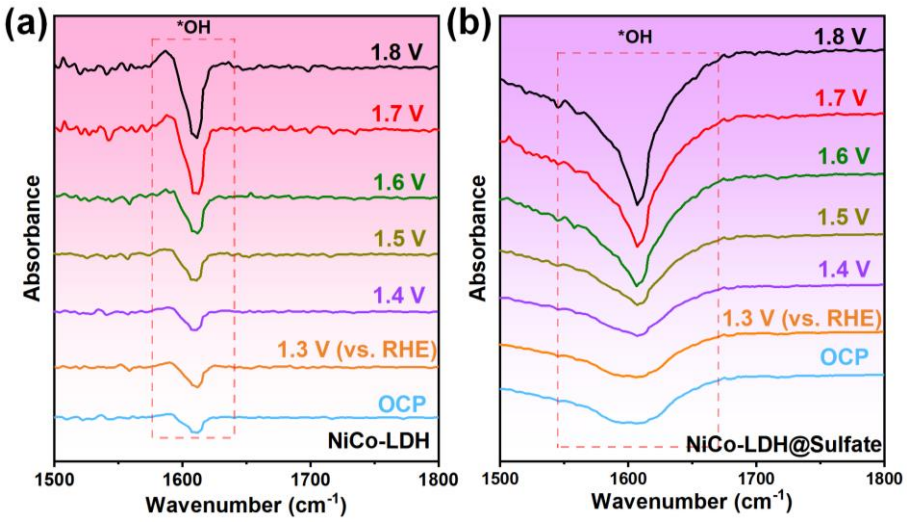

Fig. S31. (a-b) In-situ infrared spectra for NiCo-LDH (a) and NiCo-LDH@Sulfate (b) in 1 M KOH + seawater, highlighting the absorption band of *OH.

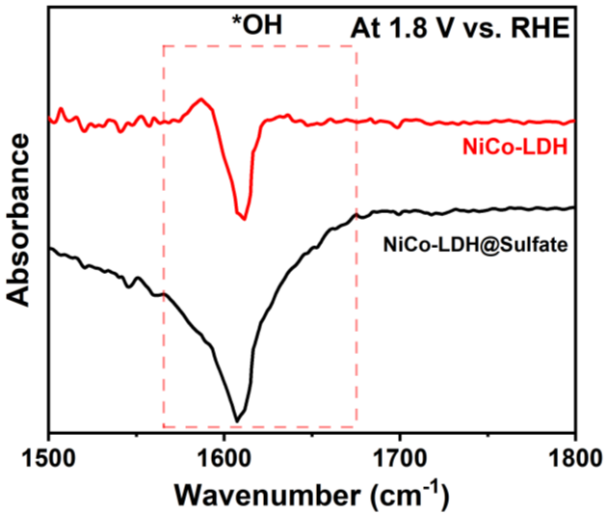

Fig. S32. (a-b) In-situ infrared spectra of NiCo-LDH (a) and NiCo-LDH@sulfate (b) at 0.8 V (vs. RHE) with highlighting the absorption band of *OH.

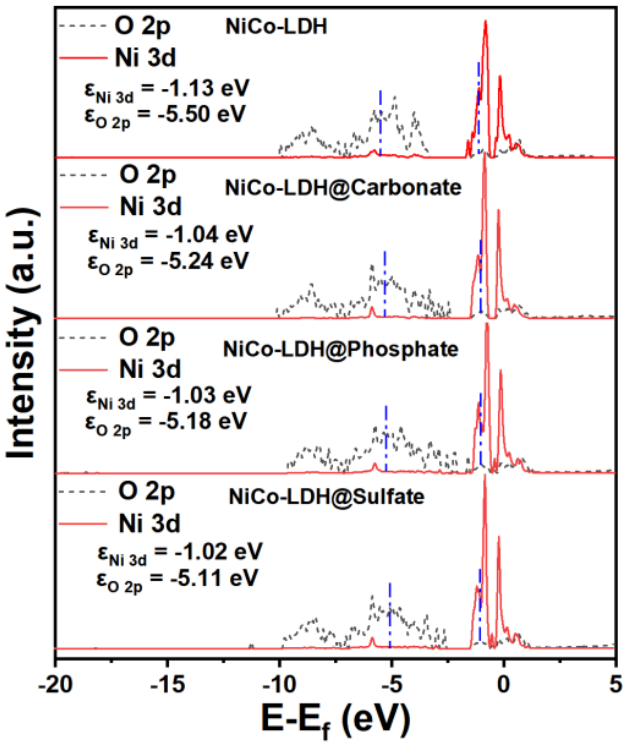

Fig. S33. PDOS plots of Ni 3d (from NiCo-LDH) and O 2p (from *OH) band for NiCo-LDH electrode modified with various oxyanion films.

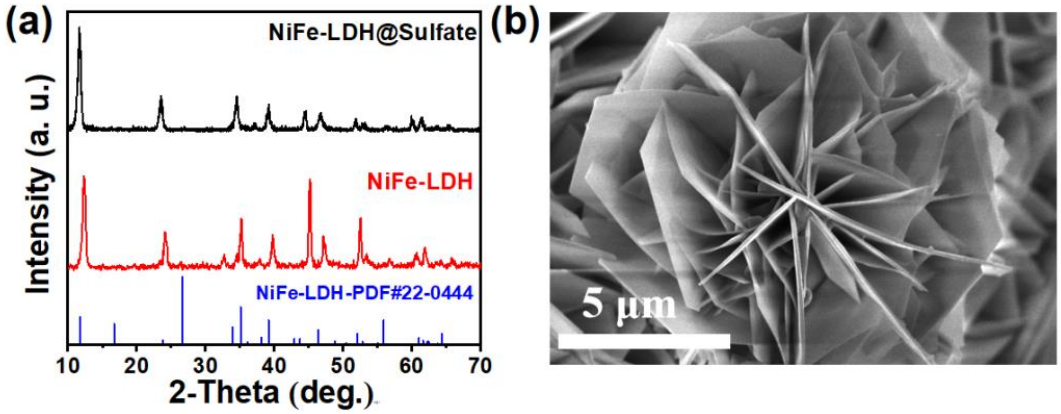

Fig. S34. (a) XRD patterns of NiFe-LDH@Sulfate and NiFe-LDH catalysts. (b) SEM images of NiFe-LDH.

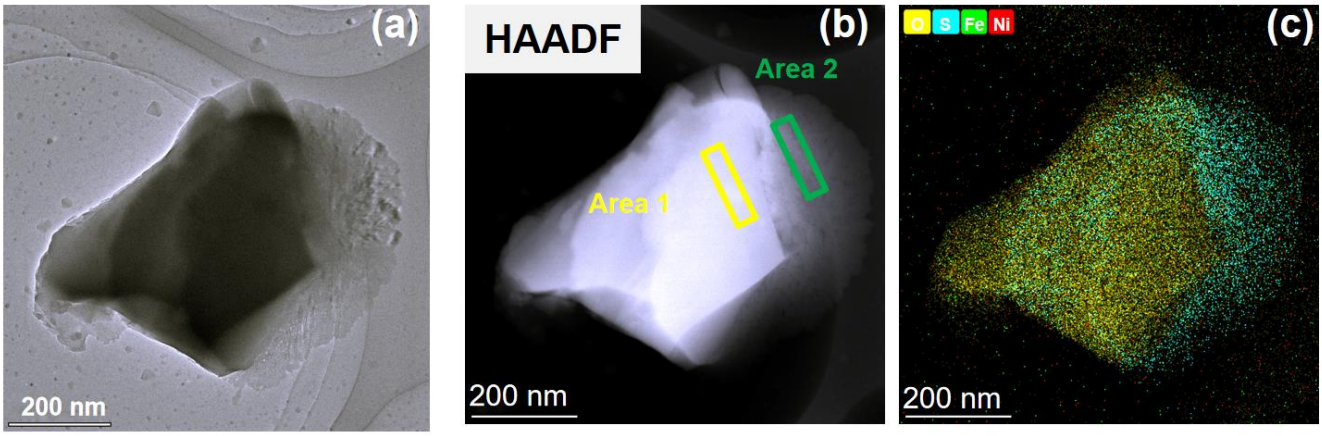

Fig. S35. TEM image (a) and EDX-mapping images (b-c) of NiFe-LDH@Sulfate.

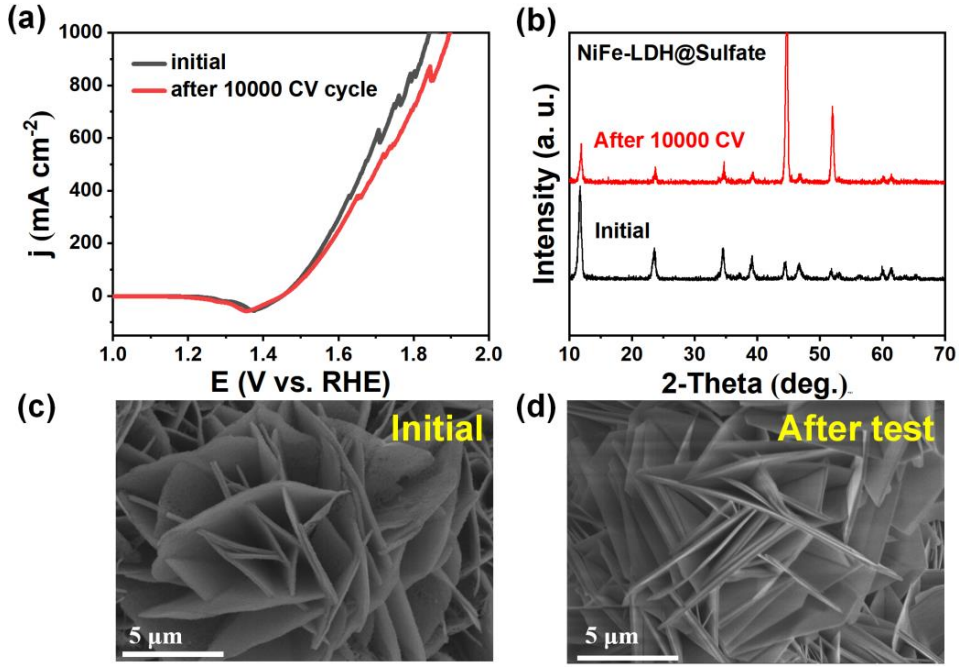

Fig. S36. Characterization of NiFe-LDH@Sulfate before and after 10000 CV cycles: LSV curves (a), XRD patterns (b), and SEM images (c-d) comparison.

After experiencing 10000 CV cycles, NiFe-LDH@Sulfate required 1.90 V to reach 1 A cm^{-2}, a mere 2.6% increase from its initial value of 1.84 V (before the test).

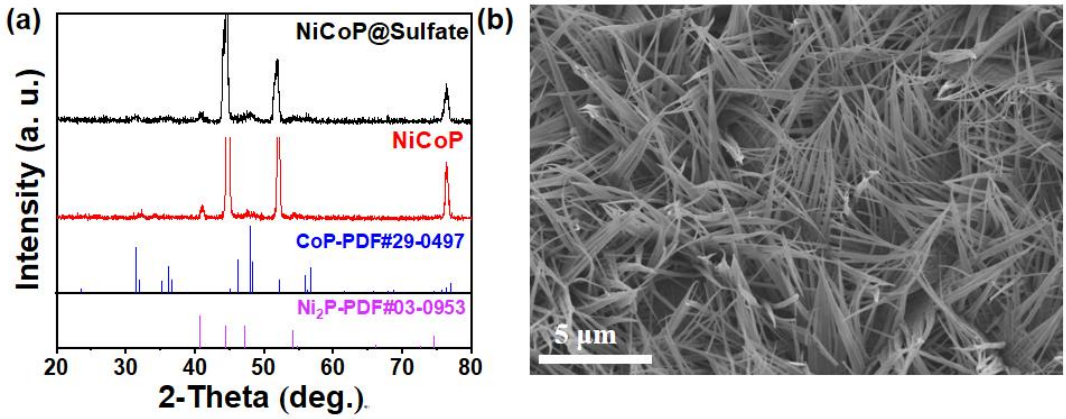

Fig. S37. (a) XRD patterns of NiCoP@Sulfate and NiCoP catalysts. (b) SEM images of NiCoP.

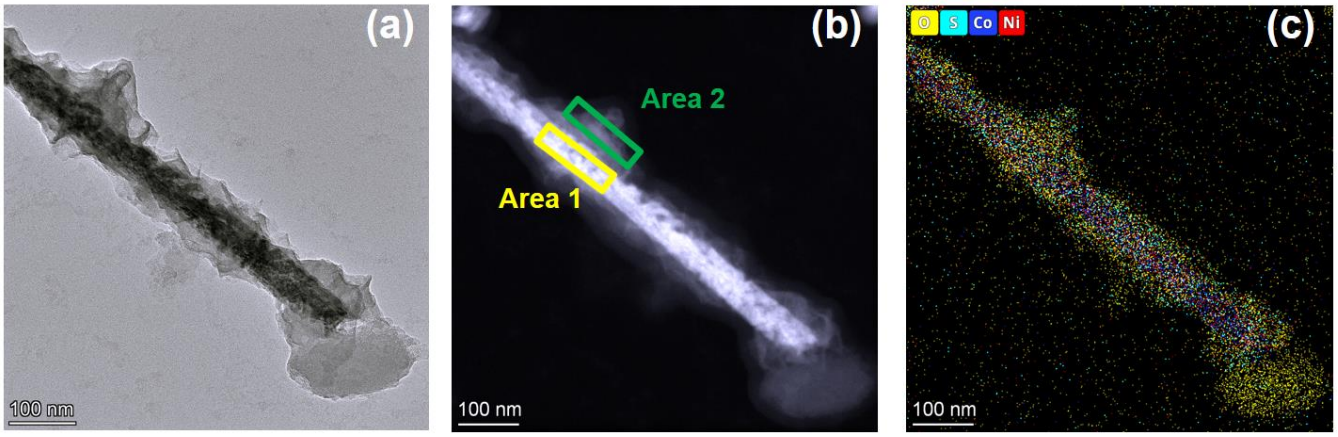

Fig. S38. TEM image (a) and EDX-mapping images (b-c) of NiCoP@Sulfate.

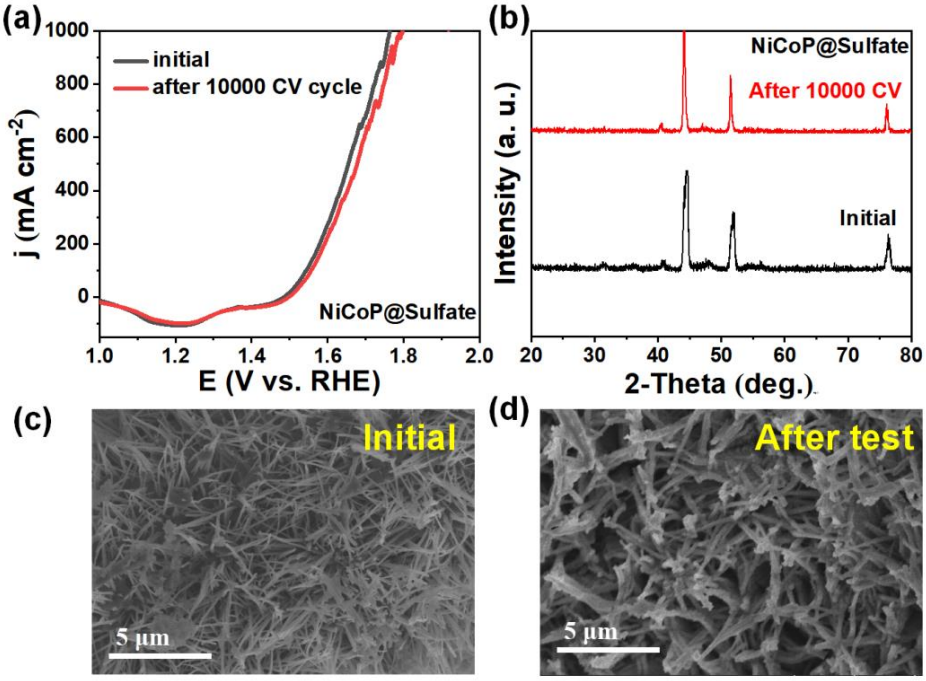

Fig. S39. Characterization of NiCoP@Sulfate before and after 10000 CV cycles: Performance comparison (a), XRD pattern (b), SEM images (c-d).

After experiencing 10000 CV cycles, NiCoP@Sulfate required 1.80 V to reach 1 A cm^{-2}, a mere 1.89% increase from its initial 1.76 V (before the test).

Table S1. Element contents in different regions of NiCo-LDH@Sulfate as measured by EDX.

	Element	**Atomic Fraction (%)**	**Mass fraction (%)**
Area 1	S	11.53	13.04
	Co	8.16	16.97
	Ni	16.39	33.92
	Element	**Atomic Fraction (%)**	**Mass fraction (%)**
Area 2	S	1.76	1.46
	Co	14.76	22.53
	Ni	37.46	56.94

Table S2. Element contents in different regions of NiCo-LDH@Phosphate as measured by EDX.

	Element	**Atomic Fraction (%)**	**Mass fraction (%)**
Area 1	P	8.57	4.95
	Co	18.93	20.28
	Ni	39.33	40.66
	Element	**Atomic Fraction (%)**	**Mass fraction (%)**
Area 2	P	1.85	1.60
	Co	22.50	28.29
	Ni	48.22	61.39

Table S3. Element contents in different regions of NiCo-LDH@Carbonate as measured by EDX.

	Element	**Atomic Fraction (%)**	**Mass fraction (%)**
Area 1	C	8.33	4.41
	Co	19.10	26.41
	Ni	41.47	49.37
	Element	**Atomic Fraction (%)**	**Mass fraction (%)**
Area 2	C	2.62	1.53
	Co	26.66	31.75
	Ni	46.01	60.73

Table S4. Comparison of the overpotentials at large current densities (η_{1000} or η_{500}) for NiCo-LDH@Sulfate with other reported OER electrocatalysts in alkaline seawater.

Catalyst	Electrolyte	Overpotential (η mV)	Ref.
NiCo-LDH@Sulfate	1 M KOH + seawater	η_{500} = 301 η_{1000} = 381	**This work**
NiMoN@NiFeN/NF	1 M KOH + seawater	η_{1000} = 398	*Nat. Commun.* **2019**, *10*, 5106.
MoO_3@CoO/CC	1 M KOH + 0.5 M NaCl	η_{800} = 650	*Nat. Commun.* **2024**, *15*, 2481.
S-Ni/Fe(OOH)/NF	1 M KOH + seawater	η_{1000} = 462	*Energy Environ. Sci.* **2020**, *13*, 3439-3446.
NiFeO-CeO_2/NF	1 M KOH + seawater	η_{1000} = 408	*ACS Nano.* **2023**, *17*, 16008-16019.
B, Fe-CoP nanofibers	1 M KOH + seawater	η_{1000} = 376	Adv. Funct. Mater. 2024, 2402264. DOI: 10.1002/adfm.2024.
Ni_2P-Fe_2P/NF	1 M KOH + seawater	η_{1000} = 431	*Adv. Funct. Mater.* **2021**, *31*, 2006484.
RuNi-Fe_2O_3/IF	1 M KOH + seawater	η_{1000} = 495	*Chin. J. Catal.* **2022**, *43*, 2202-2211.
NiFe LDH-CeW@NFF	1 M KOH + seawater	η_{1000} = 387	*Appl. Catal. B Environ.* **2023**, *330*, 122612.
NiCoS/NF	1 M KOH + seawater	η_{1000} = 470	*Appl. Catal. B Environ.* **2021**, *291*, 120071.
Ru-FeP_4/IF	1 M KOH + seawater	η_{1000} = 520	*Appl. Catal. B Environ.* **2022**, *319*, 121950.
Ru/P-$NiMoO_4$@NF	1 M KOH + seawater	η_{1000} = 510	*Appl. Catal. B Environ.* **2023**, *320*, 121977.
Fe-NiS/NF	1 M KOH + seawater	η_{1000} = 420	*Inorg. Chem.* **2023**, *62*, 7976-7981.
CoP_x@FeOOH/NF	1 M KOH + seawater	η_{500} = 377	*Appl. Catal. B Environ.* **2021**, *294*, 120256.
BZ-NiFe-LDH/CC	1 M KOH + seawater	η_{500} = 610	*Nano Res. Energy.* **2022**, *1*, 9120028.
Ni_3FeN@C/NF	1 M KOH + seawater	η_{500} = 394	*J. Mate. Chem. A.* **2021**, *9*, 13562-13569.

Table S5. The comparisons of R_s (Ω) and R_{ct} (Ω) for different electrodes.

	NiCo-LDH@Sulfate	NiCo-LDH@Phosphate	NiCo-LDH@Carbonate	NiCo-LDH
Rs (Ω)	0.92	0.98	0.97	1.02
Rct (Ω)	1.15	1.31	8.91	18.78

Table S6. Comparison of lifespan at different j for NiCo-LDH@Sulfate with state-of-the-art catalysts in alkaline seawater.

Catalyst	Electrolyte	Current density (mA cm^{-2})	Time (h)	Ref.
NiCo-LDH@Sulfate	1 M KOH + seawater	600	330	**This work**
Ni_xCr_yO	1 M KOH + seawater	500	100	*Angew. Chem. Int. Ed.* **2023**, *62*, 202309854.
NiMoN@NiFeN/NF	1 M KOH + seawater	500	24	*Nat. Commun.* **2019**, *10*, 5106.
S-Ni/Fe(OOH)/NF	1 M KOH + seawater	100	100	*Energy Environ. Sci.* **2020**, *13*, 3439-3446.
$NiCoP_v$@NF	1 M KOH + seawater	500	110	*Adv. Energy Mater.* **2024**, 2400975. DOI: 10.1002/aenm.202400975.
$NiMoO_4$@$Mo_{15}Se_{19}$/$NiSe_2$	1 M KOH + seawater	100	100	*Adv. Energy Mater.* **2024**, *14*, 2304546.
Ni (Fe)$(OH)_2$	1 M KOH + seawater	100	250	*Adv. Energy Mater.* **2023**, *13*, 2301921.
Ni_2P-Fe_2P/NF	1 M KOH + seawater	500	36	*Adv. Funct. Mater.* **2021**, *31*, 2006484.
B, Fe-CoP nanofibers	1 M KOH + seawater	100	200	*Adv. Funct. Mater.* **2024**, 2402264. DOI: 10.1002/adfm.2024.
Ni-Fe-Ce-B/MS	1 M KOH + seawater	500	100	*Appl. Catal. B Environ.* **2024**, *343*, 123560.
NiFe-LDH@Co_9S_8-Ni_3S_2/NF	1 M KOH + seawater	500	200	*Appl. Catal. B Environ.* **2024**, *354*, 124140.
CoP_x@FeOOH/NF	1 M KOH + seawater	500	80	*Appl. Catal. B Environ.* **2021**, *294*, 120256.
NiCoS/NF	1 M KOH + seawater	100	100	*Appl. Catal. B Environ.* **2021**, *291*, 120071.
B-Co_2Fe-LDH	1 M KOH + seawater	500	100	*Nano Energy.* **2021**, *83*,105838.

Fe_2O_3/NiO/NF	1 M KOH + seawater	100	50	*ACS Appl. Mater. Interfaces.* **2021**, *13*, 37152-37161
HCl-c-NiFe	1 M KOH + seawater	100	300	*Nanoscale*, **2020**, *12*, 21743-21749

Table S7. The surface element contents of NiCo-LDH@Sulfate before and after the OER reaction as determined by XPS and EDX - mapping.

Sample	Element	Atomic% (XPS)	Atomic% (EDX-mapping)
Pristine	O	48.18	54.97
	S	8.81	6.65
	Co	18.24	11.46
	Ni	24.77	26.92
After test	O	57.92	65.72
	S	5.31	4.25
	Co	14.71	8.22
	Ni	22.06	21.81

Table S8. Element contents in different regions of NiFe-LDH@Sulfate as measured by EDX.

	Element	Atomic Fraction (%)	Mass fraction (%)
Area 1	S	15.47	5.22
	Fe	26.62	31.41
	Ni	35.01	39.37
	Element	**Atomic Fraction (%)**	**Mass fraction (%)**
Area 2	S	4.66	2.89
	Fe	31.66	36.75
	Ni	42.01	50.73

Table S9. Element contents in different regions of NiCoP@Sulfate as measured by EDX.

	Element	**Atomic Fraction (%)**	**Mass fraction (%)**
Area 1	S	21.65	10.12
	Co	18.69	26.39
	Ni	39.66	56.52
	Element	**Atomic Fraction (%)**	**Mass fraction (%)**
Area 2	S	3.06	1.03
	Co	36.07	36.59
	Ni	60.27	61.38

References

1 R. Huang, Y. H. Lan, J. Chen, C. P. Li, Z. H. Zhang and M. Du, Nat. Commun., 2022, **13**, 3857.

2 N. Zhang, G. Zhang, P. Shen, H. Zhang, D. Ma and K. Chu, Adv. Funct. Mater., 2023, **33**, 2211537.

3 G. Kresse and J. Furthmüller, Phys. Rev. B., 1996, **54**, 11169−11186.

4 J. P. Perdew, K. Burke and M. Ernzerhof, Phys. Rev. Lett., 1996, **77**, 3865−3868.

5 G. Kresse and D. Joubert, Phys. Rev. B., 1999, **59**, 1758-1775.

6 P. E. Blöchl, Phys. Rev. B., 1994, **50**, 17953−17979.

7 S. Grimme, J. Antony, S. Ehrlich and H. Krieg, J. Chem. Phys., 2010, **132**, 154104.

8 G. Henkelman, B. P. Uberuaga and H. Jonsson, J. Chem. Phys., 2000, **113**, 9901.

9 Y. Kuang, M. J. Kenney, Y. Meng, W. H. Hung, Y. Liu, J. E. Huang, R. Prasanna, P. Li, Y. Li, L. Wang, M. C. Lin, M. D. McGehee, X. Sun and H. Dai, Proc. Natl. Acad. Sci. USA., 2019, **116**, 6624-6629.

10 Z. Li, Y. Yao, S. Sun, J. Liang, S. Hong, H. Zhang, C. Yang, X. Zhang, Z. Cai, J. Li, Y. Ren, Y. Luo, D. Zheng, X. He, Q. Liu, Y. Wang, F. Gong, X. Sun and B. Tang, Angew. Chem. Int. Ed., 2023, **63**, 202316522.

11 C. Hanotin, J. Puig, M. Neyret and P. Marchal, J. Nucl. Mater., 2016, **477**, 102-109.

12 X. Wang, S. Chen, C. Liu, Y. Yu, M. Xie and X. Guo, J. Energy Chem., 2022, **71**, 521-527.